Multiple unconventional Hall effects induced by noncoplanar spin textures in $SmMn_2Ge_2$

Dan Huang,[1] Hang Li,[1,2] Bei Ding,[1] Linxuan Song,[1] Xue Li,[1,3] Xuekui Xi,[1,*]
Yong-Chang Lau,[1,3] Jianrong Gao,[4] and Wenhong Wang[2,†]

[1]*Beijing National Laboratory for Condensed Matter Physics, Institute of Physics, Chinese Academy of Sciences, Beijing 100190, China*
[2]*School of Electronic and Information Engineering, Tiangong University, Tianjin 300387, China*
[3]*University of Chinese Academy of Sciences, Beijing 100049, China*
[4]*Key Laboratory of Electromagnetic Processing of Materials (Ministry of Education) Northeastern University, Shenyang 110819, China*

(Received 16 October 2023; revised 27 February 2024; accepted 22 March 2024; published 5 April 2024)

The search for materials exhibiting multiple topological transport properties such as large anomalous Hall effect (AHE) and robust topological Hall effect (THE) are crucial for novel nanospintronic devices. However, such multiple unconventional Hall responses materials are rare in nature. Here, we report the coexistence of a giant AHE and robust THE in single crystals of $SmMn_2Ge_2$ with a noncoplanar spin texture. A giant anomalous Hall conductivity of 1715 Ω^{-1} cm^{-1} is observed for $H//a$ and $I//b$ whereas a large THE is observed for $H//c$ and $I//b$. A scaling analysis suggests that the giant AHE in this compound has an overwhelmingly large extrinsic contribution due to the unconventional skew scattering induced by short-range conical spin clusters with scalar spin chirality. The large THE originates from the real-space magnetic skyrmionic bubbles which are observed using the Lorenz transmission electron microscopy. Additionally, a planar topological Hall effect (PTHE) is observed when the magnetic field and the current are coplanar. The PTHE is related to a noncoplanar spin texture with nonzero spin chirality. These observations of multiple topological transport responses contribute to a deeper understanding of the noncoplanar $SmMn_2Ge_2$ material and advance their application in spintronic devices.

DOI: 10.1103/PhysRevB.109.144406

I. INTRODUCTION

Topological materials have become the center of focus in solid-state materials research. The recent discovery of magnetic topological materials with outstanding transport responses is important for both fundamental science and the development of next-generation technological devices [1–4]. For example, the interplay between magnetism and transport properties of itinerant ferromagnets has aroused extensive interest because of a rich variety of physics and new opportunities in the design of advanced spintronic devices [5,6]. As a hallmark of spin-related transport phenomena, anomalous Hall effect (AHE) is characterized by a transverse voltage generated by a longitudinal charge current macroscopically while it is closely related to magnetic-ordering and spin-orbit coupling microscopically [7]. The AHE observed in a material can be broadly categorized into two mechanisms: intrinsic and extrinsic one. The intrinsic AHE is governed by the electronic structure of a material. The Hall conductivity of the "intrinsic" origin is closely related to the Berry curvature and thus, it has an upper limit given by e^2/ha (h and a being Planck's constant and a typical lattice constant values), typically in the order of $\sigma_{xy} = 10^2 \sim 10^3\ \Omega^{-1}\ \mathrm{cm}^{-1}$ [8]. The Berry curvature that is associated with nontrivial bands as a source of large AHE has recently been recognized in various magnetic compounds [1,2,4,9–12]. The extrinsic mechanism of AHE, on the other hand, is dependent on electrons scattering and involve the skew-scattering and side-jump scattering ones, which caused by structural defects and magnetic impurities and is not restricted by the Berry curvature [7,13]. Indeed, a recent theoretical study predicted that an unconventional giant AHE is due to the skew scattering induced by local correlation of spins [14]. Experimentally, scattering of spin clusters has been suggested to play a key role in inducement of a giant AHE. Magnetic atoms in a Kagome net of KV_3Sb_5 and chiral magnet of MnGe thin film are supposed to enhance skew scattering potential and thus, are responsible for a giant AHE [8,15]. Thus, the sign and the magnitude of the Hall conductivity dominated by the skew scattering are more related to a scalar spin chirality than to the magnetization.

On the other hand, at the adiabatic limit, itinerant spins passing through a spin texture with a finite scalar spin chirality capture an extra Berry phase in the real space. As a result, a transverse Hall voltage is induced in addition to the ordinary and anomalous Hall effects, known as a topological Hall effect (THE) [16]. The THE usually appears in the materials with a noncoplanar spin structure or a nonzero topological winding of spin textures such as skyrmions [17]. To date, a large THE has been reported in only a few topological ferromagnets [18–20], and the materials showing the coexistence of large AHE and robust THE are rare in nature, except for Kagome lattice ferromagnet Fe_3Sn_2 [21,22]. The search for materials exhibiting multiple unconventional Hall responses, i.e., large AHE and THE are crucial for novel nanospintronic

*Corresponding author: xi@iphy.ac.cn
†Corresponding author: wenhongwang@tiangong.edu.cn

devices as well as for the quest toward novel topological phenomena.

The $R$$Mn_2Ge_2$ family with various magnetism arising from both itinerant $3d$ electrons and well-localized $4f$ electrons has triggered renewed attention due to their nontrivial magnetic structure-induced THE [23–26], planar topological Hall effect (PTHE) [27], and Skyrmion bubbles [24,28]. In this family, $SmMn_2Ge_2$, the naturally noncoplanar spin structure with strong magnetocrystalline anisotropy allow it to be a possible model object for exploring multiple physical phenomena of the Hall effect. $SmMn_2Ge_2$ possesses an intricate magnetic structure where $3d$ and $4f$ moments are ordered at different temperatures [29,30]. During cooling from a paramagnetic phase, the $3d$ moments of Mn atoms are ordered into a canted ferromagnetic structure at a Curie temperature of $T_C \sim 345$ K. In this structure, the magnetic moment is oriented along the c axis accompanied by an in-plane antiferromagnetic (AFM) component. As the temperature drops to Néel temperature of $T_N \sim 150$ K, the thermal contraction-induced decrease of intralayer Mn–Mn distance leads to a conical AFM structure with both in-plane and out-of-plane AFM components. With further cooling of $SmMn_2Ge_2$ below T_N, the Sm sublattice ordered ferromagnetically, the sufficiently strong ferromagnetic (FM) coupling of Sm-Mn collapses the AFM coupling of Mn-Mn, resulting in a reentrant ferromagnetic structure [29]. Despite these changes of magnetic structure, the spin texture of the Mn sublattice remains nonlinear from T_C to the lowest temperature [30]. An analysis of the critical behavior of the ferromagnetic transition suggested that the multiple magnetic interactions exist in $SmMn_2Ge_2$ [31,32]. Despite detailed magnetic structure investigations, the transport properties of $SmMn_2Ge_2$ are poorly known. In the present work, we investigated the anisotropic magnetization and electronic transport properties of $SmMn_2Ge_2$ over a broad range of temperature. For the first time, a giant AHE for $H//a$ and a THE for $H//c$ in this $SmMn_2Ge_2$ compound have been observed and interpreted in terms of a skew scattering-dominated mechanism and real space skyrmionics bubbles, respectively. Moreover, a PTHE has been observed by applying a magnetic field and an electric current in a coplanar way. The disclosure of the multiple unusual electronic transport effects makes $SmMn_2Ge_2$ compounds promising for multifunctional applications in spintronic devices.

II. EXPERIMENTAL

Single crystal growth. Single crystals of $SmMn_2Ge_2$ were grown using an indium-flux method [27]. High-purity elemental Sm (99.9%), Mn (99.95%), Ge (99.999%), and In (99.99%) were mixed with 1:2:2:20 molar ratio in an alumina crucible. The crucible was sealed in an evacuated quartz tube to prevent the elements from oxidation at high temperature. The quartz tube was heated to 1423 K, soaked at this temperature for 24 h, and then cooled slowly to 973 K at a rate of 3 K/h. Then, the excess indium was decanted using a centrifuge. Single crystals with the platelike morphology were obtained.

Structure and Magnetic Measurements. The crystal structure of single crystals was characterized by means of a four-circle single-crystal diffractometer with Mo x-ray source and a laboratorial PANalytical Empyrean diffractometer with Cu x-ray source, respectively. The bulk composition of as-grown crystals was examined using an energy-dispersive spectrometer (EDS) attached to a Hitachi SU5000 scanning electron microscope. By means of EDS analysis, single crystals were determined to have an atomic percentage ratio of Sm: Mn: Ge close to the stoichiometry of 1: 2: 2 (Fig. S1 [33]). The atomic-scale microstructure of crystals was investigated using a JEOL ARM200F scanning transmission electron microscopy (STEM). Thermomagnetic and isothermal measurements were conducted on small pieces of a single crystal using a vibrating sample magnetometer attached to a Quantum Design superconducting quantum interference device in dc magnetic fields up to $\mu_0 H = 5$ T.

Electric transport measurements. Samples with a regular rectangular shape and a thickness of about 100 μm were cut from single crystals. Their electrical transport properties were measured using a physical properties measurement system (PPMS, Quantum Design) equipped with a sample holder allowing for sample rotation. A standard six-probe method was used to perform the resistivity measurements [34]. The Hall resistivity of the sample was symmetrized to exclude the misalignment of voltage probe. A magnetic field was applied out-of-plane ($H//c$) and in-plane ($H//a$), respectively, and always perpendicular to the electrical current direction ($I//b$) [see the inset of Figs. 3(a) and 3(b)] to measure the Hall effects. A magnetic field was rotated in-plane and out-of-plane around the c axis and a axis of samples during measurements of angle-dependent Hall effects.

Lorenz transmission electron microscopy (LTEM). Disc-shaped samples were cut from a bulk single crystal followed by mechanical and ion beam milling down to less than 100 nanometers in thickness and then fixed on a copper ring for LTEM observations. Magnetic domains were observed using a JEOL 2100F transmission electron microscope in the Lorentz TEM mode. Images were captured under three focusing conditions, under-focus, over-focus and accurate (or zero) focus using a charge-coupled device camera attached to the LTEM. The morphology and sizes of magnetic domains at room temperature was investigated with and without a magnetic field.

III. RESULTS

A. Crystal structure and magnetization

The results from the four-circle single-crystal diffractometer revealed that the $SmMn_2Ge_2$ crystalizes into a $ThCr_2Si_2$−type tetragonal structure with the space group I4/mmm. The lattice parameters are $a = 4.066(3)$ Å, $b = 4.066(3)$ Å, and $c = 10.906(9)$ Å at room temperature, which is agreement with the previous report by a powder x-ray diffraction [35]. More information about the crystal structure, the various crystal planes and the diffraction spots on the main crystallographic direction of the $SmMn_2Ge_2$ single crystal are shown in Table S1 and Fig. S2 [33]. As illustrated in Fig. 1(a), layers of Sm, Mn and Ge atoms are stacked along the c axis following the sequence of −Sm−Ge−Mn−Ge−Sm−. The Mn and Sm atoms within the ab plane constitute a square-shaped framework in their respective layer [Fig. 1(b)]. The nearest Mn-Mn intralayer distance given by $a/\sqrt{2}$ is smaller

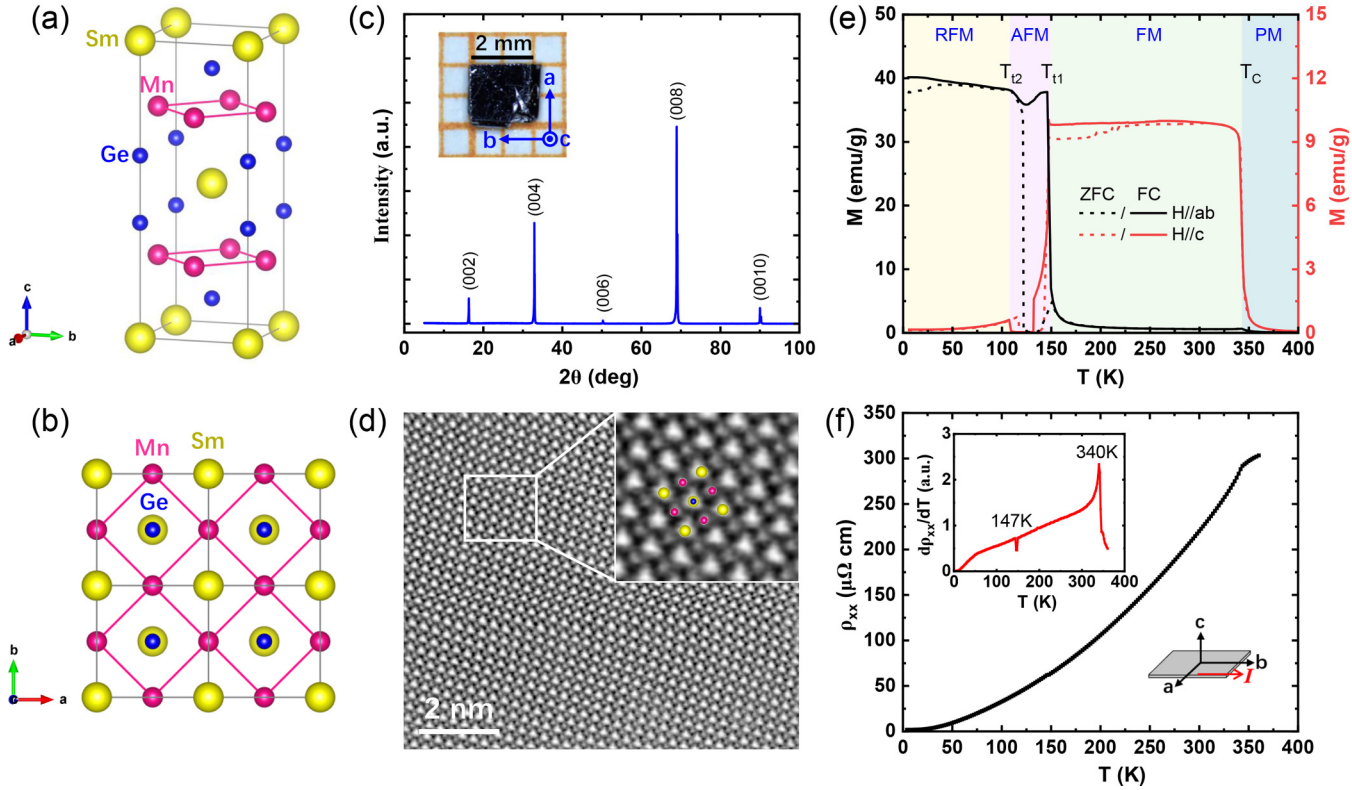

FIG. 1. (a) and (b) Schematic illustration of the crystal structure of $SmMn_2Ge_2$ viewed from the side and the top. (c) The XRD pattern of a single crystal with the a (00l) plane exposed to the surface. The inset shows the typical morphology of a single crystal. (d) High-resolution lattice image taken from the [00l] axis using STEM. (e) The temperature dependences of magnetization under zero-field cooling (ZFC) and field cooling (FC) in a magnetic field of 0.01 T with $H//c$ and $H//ab$. (f) Temperature dependence of in-plane zero-field resistivity. Top inset: derivative of resistivity relative to temperature. Bottom inset: a schematic illustration showing the direction of an electric current relative to primary crystallographic axes.

than that of interlayer separation c/2 [35]. The morphology of a single crystal is shown in the inset of Fig. 1(c) and it has a size of about $2 \times 2 \times 0.2\,mm^3$. It was determined using x-ray diffraction (XRD) analysis that the rectangular crystal surface is the *ab* plane of the tetragonal crystal lattice. As shown in Fig. 1(d), high resolution imaging using STEM reveals that the crystals are free of obvious crystal defects, indicating high quality. As shown in Fig. 1(e), zero-field-cooling (ZFC) and field-cooling (FC) curves of a $SmMn_2Ge_2$ single crystal in magnetic fields of $\mu_0 H = 0.01$ T parallel to the *c* axis ($H//c$) and the *ab* plane ($H//ab$) indicate three thermally induced magnetic transitions in sequence of decreasing temperature: a FM transition of Mn sublattice at $T_C \sim 343$ K, an AFM transition of Mn sublattice at $T_1 \sim 150$ K, and a reentrant FM transition at $T_2 \sim 108$ K. These transitions are in good agreement with determined for a polycrystalline material of the same bulk composition [29,30]. The ZFC and FC curves are separated from each other in $H//c$ at low temperatures. This behavior is typical for frustrated ferromagnets indicating the formation of a spin-frozen phase [34]. The magnitude of magnetization with $H//c$ is larger than that with $H//ab$ at high temperatures but it becomes smaller than that with $H//ab$ at low temperature. These opposing trends indicate a switch of the easy magnetization direction from the *c* axis to the *ab* plane. As shown in Fig. 1(f), the resistivity ρ_{xx}(T) under zero field in the temperature range of 4−380 K indicates a typically metallic behavior. The derivative of resistivity relative to temperature, shown in the inset of Fig. 1(f), indicates sharp changes at 340 K and 147 K, which coincide with the paramagnetic (PM) to FM and the FM to AFM transitions, respectively.

B. Magnetocrystalline anisotropy of single crystals

As shown in Fig. 2(a), isothermal magnetization curves measured with $H//a$ axis show a ferromagnetic behavior at temperatures above 160 K. The isothermal magnetization curves show a field-induced spin-flop-type metamagnetic transition of first order from an AFM state to a FM state at the temperatures 120 K and 130 K. This observation is agreement with the previous studies [31,32]. At lower temperatures, the metamagnetic transition is not observed. Instead, magnetization increases sluggishly with increasing field up to a high field of 5 T. This sluggish magnetization behavior is consistent with the AFM ground state along the *c* axis [29,30]. In contrast, the magnetization curves measured with $H//ab$ at temperatures above 160 K show a nonlinear field dependence before saturation. This nonlinear field dependence is expected for a typically conical spin structure and it indicates the formation of a magnetic noncoplanar lattice similar to that of $PrMn_2Ge_2$ [27]. A spin-flop-type metamagnetic phase transition is observed at 130 K. Although this transition resembles

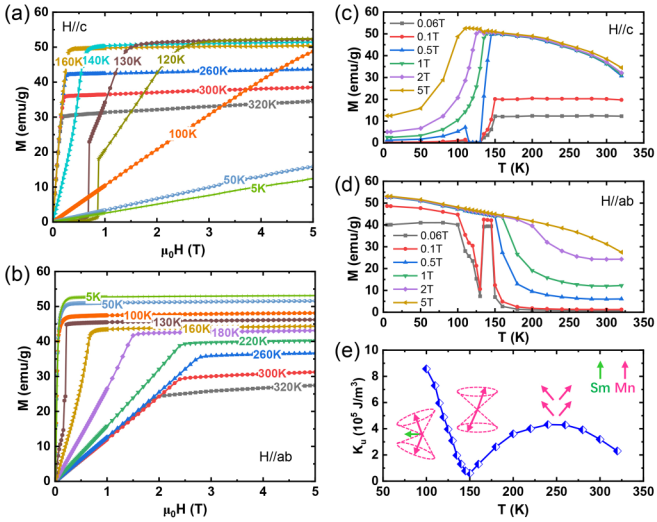

FIG. 2. Isothermal magnetization M(μ_0H) curves for (a) $H//c$ axis and (b) $H//ab$ plane. Temperature dependences of isothermal magnetization at different fields with (c) $H//c$ axis and (d) $H//ab$ plane. (e) Temperature dependence of magnetocrystalline anisotropy constant (K_u). The insets are schematic illustrations of the spin configurations at different temperature regions determined using neutron scattering [30].

that observed with $H//c$ at the same temperature, there are also differences. The jump of magnetization is larger and the critical field driving the transition is lower. These differences are consistent with the characteristics of field-induced spin-flop processes [32]. The magnetization at 2 K is saturated in a low magnetic field, suggesting an in-plane FM behavior. The easy magnetization direction of the single crystal of $SmMn_2Ge_2$ can be determined in terms of isothermal magnetization curves with the $H//c$ and $H//ab$. At temperature above 160K, the easy magnetization direction is along the c axis because saturation of magnetization is attained at a lower field with $H//c$ direction than with $H//ab$. As temperature decreases to 130 K, the easy magnetization direction is changed from the c axis to the ab plane because the critical field for saturation of magnetization becomes higher with $H//c$ than with $H//ab$. Figs. 2(c) and 2(d) show the temperature dependence of magnetization extracted from the isothermal measurements with $H//c$ and $H//a$. The temperature dependence of magnetization at a low field shows the same trends as those revealed by the thermomagnetic curves of Fig. 1(e). The sharp changes of magnetization at characteristic temperatures are consistent with the thermally induced changes of the magnetic structures determined using neutron scattering [30]. It is noted that the AFM transition and the AFM-FM transition both are suppressed by a magnetic field of 1 T and 0.5 T for $H//c$ and $H//ab$, respectively. The difference between the critical fields indicates strong magnetocrystalline anisotropy.

The magnetocrystalline anisotropy constant can be approximated using the formula of $K_u = H_K M_S/2$ [36], where M_S is the saturation magnetization and H_K is the anisotropy field defined as a critical field above which the magnetization along the two magnetic field directions ($H//c$ and $H//a$) becomes consistent with each other. The magnetocrystalline anisotropy constant evaluated against temperature is plotted in Fig. 2(e). For convenience, the arrangements of magnetic moments of Mn and Sm atoms of $SmMn_2Ge_2$ at different temperatures are schematically shown in the inset of Fig. 2(e). During cooling from the T_C, the magnetocrystalline anisotropy constant increases with decreasing temperature first. This trend is reversed after a maximum of the magnetocrystalline anisotropy constant is attained at ~250 K. In this near-room temperature region, the bulk magnetism of the compound is dominated by the canted ferromagnetic structure of Mn atoms whereas the contribution by the magnetic moment of Sm atoms is negligible [30]. As temperatures below 150 K, the magnetocrystalline anisotropy constant increases with decreasing temperature. In the temperature range 100−150 K, moments of Mn atoms have a conical antiferromagnetic configuration, though those of Sm atoms are not ordered yet. Thus, the increase of the magnetic anisotropy constant can be attributed to a continuous change of the conical angle between the antiferromagnetically coupled magnetic moments of Mn atoms. At temperatures below 100 K, the magnetocrystalline anisotropy constant was not estimated because the magnetization with $H//c$ is not saturated at a high magnetic field of 5 T due to the AFM state. However, it should be larger than at 100 K.

C. Anomalous Hall effect

Figures 3(a) and 3(b) show the magnetic-field dependence of the Hall resistivity ρ_{zx} and ρ_{yx} at various temperatures for $H//a$ and $H//c$, respectively. The Hall resistivity exhibits a significant AHE near room temperature. The AHE is weakened with decreasing temperature due to a reduction of resistivity. The anomalous Hall resistivity in magnetic fields with $H//a$ and $H//c$ disappears at temperatures below 40 and 100 K, respectively. These changes are understood because the ordinary Hall effect dominates at low temperatures (see Figs. S3 and S4 for more detail [33]). The slope of ρ_{zx} is positive at 5 K but that of ρ_{yx} is negative. This difference suggests that holes and electrons are the dominant mechanism of Hall resistivity with $H//a$ and $H//c$, respectively. In other words,

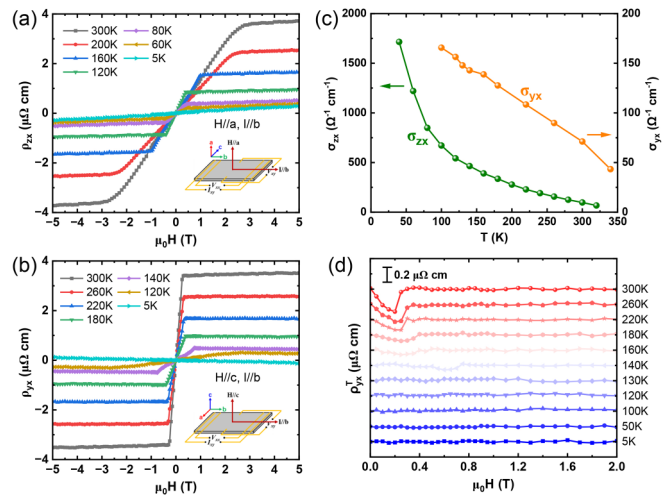

FIG. 3. Anomalous Hall resistivity in a magnetic field applied along (a) the a axis and (b) the c axis. (c) Temperature dependences of AHC with $H//a$ and $H//c$. (d) Field dependence of topological Hall resistivity with $H//c$.

TABLE I. Comparison of maximum THE showing at corresponding temperature for different bulk materials.

Materials	Ground state	Mechanism of THE	Max THE ($\mu\Omega$ cm)	Temperature (K)	Ref.
MnSi	Helimagnet	Skyrmion	0.004	28.5	[42]
MnGe	Helimagnet	Skyrmion	0.16	30	[43]
$Mn_{1.4}PtSn$	Noncoplanar ferromagnet	Antiskyrmion	0.9	2–135	[44]
MnNiGa	Ferromagnet	Bubble-type skyrmion	0.15	300	[45]
Mn_3X X = (Ga, Sn, Ge)	Noncollinear antiferromagnet	Spin chirality	0.25–3.0	2–90	[46–48]
Fe_3GeTe_2	Ferromagnet	Bubble-type skyrmion	2.04	100	[49]
Fe_3Sn_2	Frustrated magnet	Spin chirality	0.875	380	[41]
Fe_5Sn_3	Frustrated magnet	Spin chirality	2.12	350	[50]
$TbCo_2$	Noncoplanar ferrimagnet	Spin chirality	0.4	232	[34]
$DyCo_2$	Noncoplanar ferrimagnet	Spin chirality	0.6	142	[34]
YMn_6Sn_6	Helical antiferromagnet	Spin chirality	2.0	240	[51]
$TmMn_6Sn_6$	Helical antiferromagnet	Spin chirality	1.3	250	[52]
$LaMn_2Ge_2$	Noncoplanar Ferromagnet	Spin chirality	1.0	190–300	[23]
$NdMn_2Ge_2$	Noncoplanar Ferromagnet	Skyrmion	2.05	210	[24]
$SmMn_2Ge_2$	Noncoplanar Ferromagnet	Bubble-type skyrmion	0.3	300	This work

holes and electrons both exist in the $SmMn_2Ge_2$ compound and their concentrations can be tuned by changing the direction of a magnetic field applied. A similar mechanism has been suggested for the Hall resistivity of $LiMn_6Sn_6$ [37]. The opposite signs of the Hall effect along different axis suggest that the $SmMn_2Ge_2$ might be a goniopolar material with a hyperboloid open Fermi surface like $NaSn_2As_2$ [38,39]. This possibility needs to be checked using band structure calculations. The anomalous Hall conductivity (AHC) σ_{zx} and σ_{yx} with $H//a$ and $H//c$ was calculated using the formula of $\sigma^A_{yx} = -\rho^A_{yx}/[\rho^2_{xx} + (\rho^A_{yx})^2]$, where ρ^A_{yx} and ρ_{xx} are the anomalous Hall resistivity and the longitudinal resistivity at zero field, respectively. As shown in Fig. 3(c), the AHC in both directions increases with decreasing temperature. The maximum of AHC with $H//a$ and $H//c$ are 1715 Ω^{-1} cm^{-1} and 166 Ω^{-1} cm^{-1}, which are attained at 40 and at 100 K, respectively. While these values show an anisotropic AHE, the former indicates a giant AHC, which is even larger than that the upper threshold of AHC set by the intrinsic mechanisms related to the Berry curvature [8]. To repeat this giant AHC, we did measurements on another single crystal sample with $H//a$. Even a larger value of AHC, 1860 Ω^{-1} cm^{-1}, was attained at 40 K (see Fig. S5 [33]). Thus, the giant and anisotropic AHE in the single crystals of $SmMn_2Ge_2$ is verified. This giant and anisotropic AHC suggests a drastic change of the electronic structure of $SmMn_2Ge_2$ by the magnetic field applied and this origin is discussed in the following section.

D. Topological Hall effect

A significant topological Hall effect (THE) signal was extracted from the measurements in addition to a conventional AHE with $H//c$. For a magnetic system, Hall resistivity ρ_{xy} can be divided into three parts using the formula $\rho_{xy} = R_0B + R_SM + \rho^T_{xy}$ [7], where R_0 is the ordinary Hall coefficient, R_S is the anomalous Hall coefficient, M is magnetization, and ρ^T_{xy} is the topological Hall resistivity. Fitting this expression into the data measured (Figs. S4e-f [33]), we established the field dependence of ρ^T_{xy} as shown in Fig. 3(d). The data in low fields shows a negative maximum of 0.3 μΩ cm at 300 K, indicating a large THE. This THE is most likely to be induced by a skyrmion spin texture. It is weakened with decreasing temperature and finally vanishes below 140 K. The vanishing of the THE can be related to the change of the easy magnetization direction from the c axis to the ab plane. The THE in $SmMn_2Ge_2$ is robust at room temperature. A similar THE has been reported for centrosymmetric magnets $LaMn_2Ge_2$ [23], $NdMn_2Ge_2$ [24], Ni_2MnGa [40], and Fe_3Sn_2 [41]. The existence of THE in centrosymmetric magnets can be attributed to the formation of Skyrmionic bubbles as the result of a competition between magnetic dipole interaction and an uniaxial magnetocrystalline anisotropy [40]. Table I lists the THE reported for various materials. The THE of $SmMn_2Ge_2$ is comparable to that of $TbCo_2$ and $DyCo_2$ [34]. While these two compounds have strong $4f - 3d$ interactions in their ferrimagnetic lattices, they are more expensive than the title compound because of a higher concentration of rare earth elements. The THE of $SmMn_2Ge_2$ is smaller than in $LaMn_2Ge_2$ [23] and $NdMn_2Ge_2$ [24], but it is robust at ambient temperature. In fact, it is also larger than that reported for the other Skyrmion-hosting material such as MnSi and MnGe [42–45]. Thus, it is more promising for technological applications in spintronic devices.

E. Planar topological Hall effect

Apart from magnetotransport properties with H perpendicular to the current, the Hall resistivity in the ab plane was also investigated by rotating the H in the bc and ab

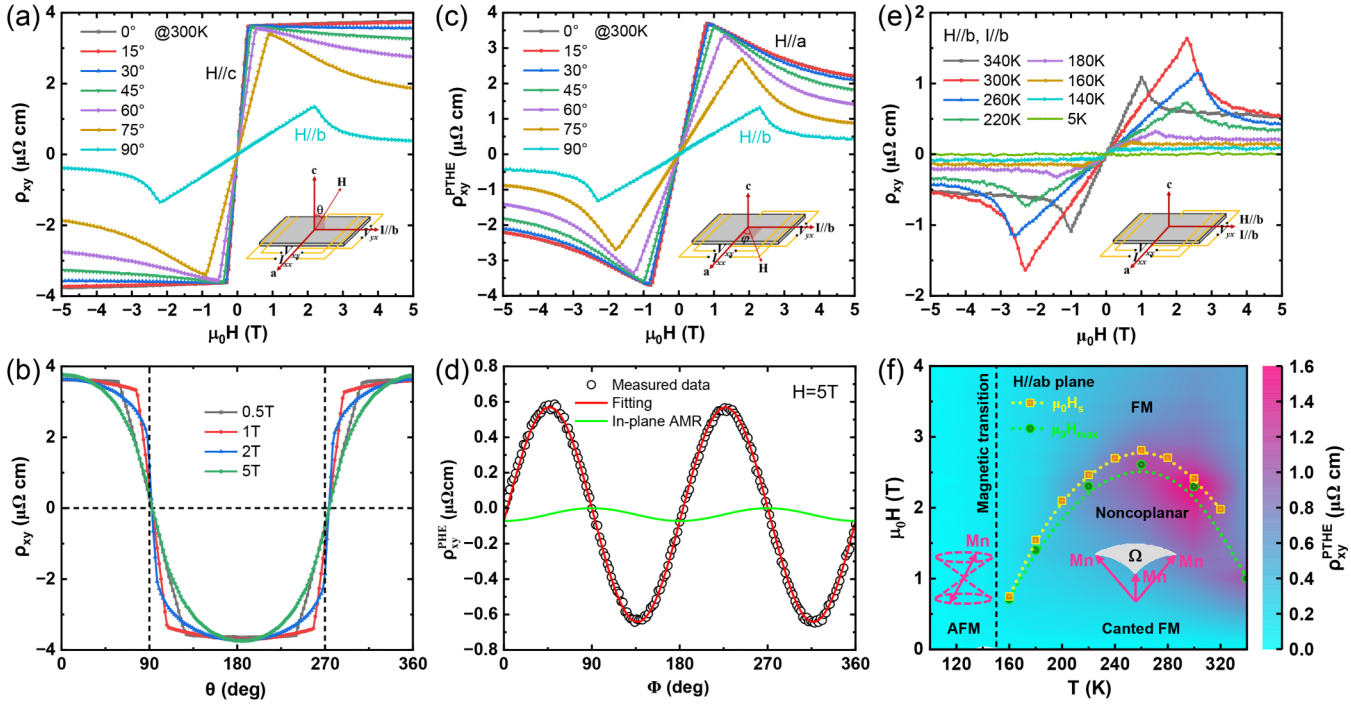

FIG. 4. (a) Magnetic field dependence of ρ_{xy} measured out of the *ab* plane with H in the direction of $\theta = 0°$, 15°, 30°, 45°, 60°, 75°, and 90° at 300 K. (b) Angular dependence of ρ_{xy} at 300 K under a magnetic field of 0.5 T, 1 T, 2 T, and 5 T. (c) Magnetic field dependence of in-plane ρ_{xy} at $\varphi = 0°$, 15°, 30°, 45°, 60°, 75°, and 90° at 300 K. (d) Angular dependence of ρ_{xy} at 300 K under a magnetic field of 5 T. (e) Planar topological Hall resistivity with $H//b$. (f) Magnetic phase diagram of $SmMn_2Ge_2$ above 100 K. The yellow solid circles show the critical magnetic fields for attaining a maximum ($\mu_0 H_{max}$) of the planar topological Hall resistivity. The inset of (f) shows the schematic spin configurations of Mn moments in a canted FM and in an AFM state.

plane. Firstly, a magnetic field was rotated from the *c* axis to the *ab* plane as shown in the Fig. 4(a). An angle between the magnetic field and the *c* axis is denoted as θ for convenience. A large anomalous Hall resistivity was observed when $\theta = 0°$. This result is consistent with the measurement of the Hall resistivity using the conventional method [see Fig. 3(b)]. As θ is increased from 0° to 90°, ρ_{xy} is reduced. However, a pronounced cusplike anomaly is observed in a low field region. The cusp is distinct especially when $\theta = 90°$. Whereas a difference between the measured and actual angles of H and I is negligible, ρ_{xy} determined for different magnetic fields converges to zero at angles of 90° and from 270° with a scatter of less than 5° [Fig. 4(b)]. Therefore, the cusplike anomaly is observed when a magnetic field and an electric current are coplanar. This anomaly resembles another topological signal, termed the PTHE [53]. The PTHE has been observed only in a few skyrmion-hosting materials including $PrMn_2Ge_2$ [27], Cr_5Te_8 [54], and Fe_3GeTe_2 [49] until now. It has been generally attributed to a nonzero spin chirality, in which a noncoplanar spin texture offers an effective gauge field to yield an exotic planar Halllike signal. A smooth cosine dependence is observed at a high magnetic field of $\mu_0 H = 5$ T only. At lower fields, e.g., $\mu_0 H = 0.5$ T, 1 T and 2 T, deviations from the cosine angular dependence are significant across the 90° and 270° due to a large topological Hall signal.

To verify the PTHE nature of the low-field cusplike anomaly, we carried out a detailed in-plane angle-dependent measurements with the field rotated in the *ab* plane of a single crystal at 300 K. Here, an angle between H and I in the *ab* plane is denoted as φ [see the inset of Fig. 4(c)]. The PTHE is reduced during a sweeping of φ from 0° to 90°, indicating the in-plane anisotropy of the PTHE. Like $PrMn_2Ge_2$ [55], $SmMn_2Ge_2$ is magnetically isotropic within the *ab* plane. Then, a large anisotropy of the PTHE is probably caused by a change of the direction of the current. That is, the PTHE exists in any direction at low magnetic fields in spite of the anisotropy when H is rotated in the *ab* plane. Here, the PTHE is viewed as an intrinsic phenomenon for noncoplanar magnets following recent experimental and theoretical studies [27,53], and it has little to do with the in-plane anisotropic magnetoresistance (AMR). To verify this hypothesis, we measured the angular-dependent PHE in a saturating field of 5 T at 300 K, in a ferromagnetic state and is plotted in Fig. 4(d). The PHE was obtained using the formula $[\rho_{xy}(+H) + \rho_{xy}(-H)]/2$ to eliminate the misalignment of the Hall voltage probe. The planar Hall resistivity $\rho_{xy}^{PHE}(\varphi)$ was obtained by subtracting the longitudinal resistance offset. The latter follows $\rho_{xy}^{PHE}(\varphi) = -\Delta\rho_{xy} \sin\varphi \cos\varphi + a\Delta\rho_{xy}\cos^2\varphi$, where $\Delta\rho_{xy} = \rho_{\perp} - \rho_{//}$ with $\rho_{\perp}$ and $\rho_{//}$ are the resistivity measured when the electric and magnetic fields were applied in a perpendicular and a parallel direction, respectively [56,57]. The first term of the longitudinal resistance offset is the intrinsic PHE and the second term is the in-plane AMR. By fitting the formula of the longitudinal resistance offset to the planar Hall resistivity, we obtained the in-plane AMR which is shown by the green line in Fig. 4(d). The PHE characterized by the transverse Hall resistivity was fitted using a formula proposed by Li *et al.*

[57]. Then, the in-plane AMR and intrinsic PHE contribution were separated from each other. The AMR of $SmMn_2Ge_2$ shows a maximum of 0.16% compared to the total planar Hall resistivity, which is negligible compared to the AMR for conventional transition metal compounds [58,59]. Thus, the PTHE of $SmMn_2Ge_2$ is intrinsic.

Finally, we measured the in-plane Hall resistivity ρ_{xy} during cooling of the single crystal from 340 to 5 K by setting $\theta = 90^\circ$, i.e., H//I, as shown in Fig. 4(e). The PTHE signal of ρ_{xy} is strongest at 300 K and it remains discernible down to 160 K. The PTHE signal vanishes at lower temperatures, which may be related to the decrease of resistivity with temperature or the change of the easy magnetization. In terms of the magnetoelectric transport properties measured, we propose a magnetic phase diagram for $SmMn_2Ge_2$ at temperatures between 100 K and T_C [Fig. 4(f)]. The phase diagram displays temperature dependences of a critical magnetic field ($\mu_0 H_{max}$) for attaining the maximum of PTHE and a saturating magnetic field ($\mu_0 H_S$) applied in the *ab* plane [see Fig. 2(b)]. The critical field and the saturating field both increase with increasing temperature first and then, they decrease after passing a maximum at about 260 K. These trends in temperature dependence are similar to those determined for the magnetocrystalline anisotropy constant and can be related to the spin moments of 3*d* electrons of Mn atoms. The phase diagram also highlights that a noncoplanar magnetic structure is established upon the application of an in-plane magnetic field smaller than $\mu_0 H_S$. Here, the noncoplanar magnetic structure introduces a nonzero spin chirality which is responsible for the PTHE in $SmMn_2Ge_2$ as it does in magnetically frustrated systems [49,54]. Once the magnetic field applied exceeds the critical field ($\mu_0 H > \mu_0 H_S$) at a given temperature, the spins of Mn atoms with the canted ferromagnetic structure will arrange themselves in a parallel way. Then, the noncoplanar magnetic structure is suppressed and so is the PTHE.

IV. DISCUSSION

To understand the origin of the AHE in the $SmMn_2Ge_2$, we check the scaling behavior of $\rho^A_{yx(zx)}$ using the relation $\rho^A_{yx(zx)} \propto \rho^\alpha_{xx}$ [60]. As shown in Fig. 5(a), a scaling law parameter of $\alpha = 1.33$ is obtained by plotting ρ^A_{xy} against ρ_{xx} on log-log scaling for *H//a*. This value of α confirms that the AHE includes an extrinsic and an intrinsic contribution. The total anomalous Hall resistivity usually includes extrinsic contributions, given by skew scattering and side jumps scattering, and an intrinsic contribution. Skew scattering at impurities is responsible for an AHE, which gives $\rho_{sk} \propto \rho_{xx}$ [61]. The side jump at impurities also makes a contribution to the AHE and it accounts for the relation $\rho_{sj} \propto \rho^2_{xx}$ [62]. The intrinsic contribution accounts for an anomalous velocity in the direction transverse to the electric field, which gives $\rho_{int} \propto \rho^2_{xx}$ [63]. Thus, the total anomalous Hall resistivity can be written as $\rho^A_{yx(zx)} = \rho_{sk} + \rho_{sj} + \rho_{int} = \alpha\rho_{xx} + \beta\rho^2_{xx} + \gamma\rho^2_{xx}$, where α, β, and γ are the resistivity coefficients. However, it is difficult to distinguish the last two items on the right side of this

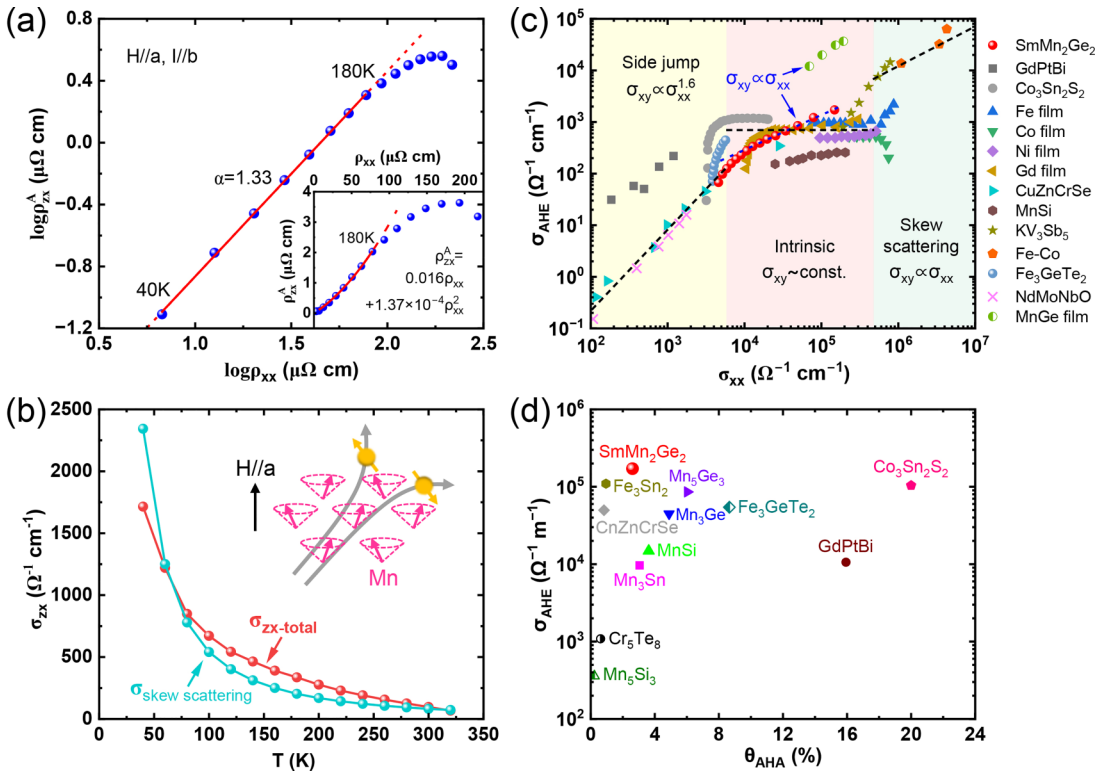

FIG. 5. (a) Plot of log (ρ^A_{zx}) vs log (ρ_{xx}). The inset of (a) shows the plot of ρ^A_{zx} vs ρ_{xx}. (b) Temperature dependence of σ_{zx} and $\sigma_{skew-scattering}$. (c) Log-log plot of σ_{AHE} versus σ_{xx} for various materials. Note that the large Hall conductivity and the Hall angle realized in $SmMn_2Ge_2$ show significant deviations from the conventional scaling plots. The data of other materials are taken from literature [8,64–67]. These scaling relations are shown by black dashed lines. (d) σ_{AHE} versus σ_{xx} of various metallic ferromagnets and semimetals [1,2,64–66,68–71].

formula because they both conform to the squared relation of the longitudinal resistivity. Nevertheless, it can be seen from the fitting results of the inset of Fig. 5(a) that the skew scattering directly proportional to longitudinal resistivity plays an overwhelming role in anomalous Hall resistivity. Here, we focus attention on the linear item, i.e., the contribution by the skew scattering. The extrinsic skew scattering contributed to the AHC can be obtained by formula of $\sigma^A_{zx,sk} \approx \frac{\alpha\rho_{xx}}{\rho^2_{xx}}$. As shown in Fig. 5(b), $\sigma^A_{zx,sk}$ plays a dominant contribution to the total Hall conductivity, especially at low temperatures. The AHC of σ^A_{yx} for $H//c$ has also been analyzed (see Fig. S6 for details [33]). However, the σ^A_{yx} is dominated by an intrinsic mechanism, which has a common origin with the AHE of $PrMn_2Ge_2$ [27]. The different dominant mechanism of AHC for $H//a$ and $H//c$ also suggests that $SmMn_2Ge_2$ is likely to be a goniopolar material [38,39].

The AHE in $SmMn_2Ge_2$ and that in other materials are shown in Fig. 5(c) for comparison. The AHE is divided into three regimes from the side jump ($\sigma_{xy} \propto \sigma^{1.6}_{xx}$) through the intrinsic ($\sigma_{xy} \sim$ const.) to the skew scattering ($\sigma_{xy} \propto \sigma_{xx}$) [64]. The red solid circles show the AHE of the $SmMn_2Ge_2$ compound, which conforms to the skew scattering mechanism as indicated by a linear dependence on σ_{xx}. The AHC of $1.7 \times 10^3\ \Omega^{-1}\,cm^{-1}$ in $SmMn_2Ge_2$ is comparable with that attained in $Co_3Sn_2S_2$ [4] with an intrinsic mechanism. Thus, we term it as a giant AHC. So far, a giant AHC value has been observed in a few materials only. We noted that the anomalous Hall conductivity dominated by the skew scattering cannot reach this regime according to the division of experience regimes. This case is similar to the recent reported large AHE dominated by extrinsic skew scattering mechanism in the materials of Kagome magnets KV_3Sb_5 ($\sigma_{AHE} \sim 1.55 \times 10^4\ \Omega^{-1}\,cm^{-1}$) [15] and MnGe thin films with the spin chirality cluster ($\sigma_{AHE} \sim 4 \times 10^4\ \Omega^{-1}\,cm^{-1}$) [8]. The giant AHC in the latter materials have been attributed to an unconventional skew-scattering mechanism. In this mechanism, spin clusters with scalar spin chirality are thermally activated as indicated by the temperature and magnetic-field profile of the AHE in thin film or materials with a magnetocrystalline anisotropy [14]. Thus, the giant AHE in $SmMn_2Ge_2$ can be attributed to the same mechanism. As shown in the inset of Fig. 5(b), conical spin clusters of Mn atoms are similar to those of a Kagome net and it can behave like a "magnetic scattering center", generating an enhanced skew scattering by introducing a distortion of the local order and therefore a net magnetization to act as scattering centers in an external field. The anisotropy of the Hall response of σ_{zx} and σ_{yx} for $H//a$ and $H//c$ also strongly supports the spin chirality skew-scattering mechanism suggested above. The giant AHE in the $SmMn_2Ge_2$ compound may have another origin. That is, the magnetocrystalline anisotropy enlarged at low temperatures might bring about a magnetic crossing node in the momentum space. Investigation of the electronic structure using angle-resolved photoemission spectroscopy and theoretical calculations can help verify this hypothesis. Figure 5(d) is a plot of the σ_{AHE} against anomalous Hall angles ($\theta_{AHE} = \sigma^A_{xy}/\sigma_{xx}$) for representative ferromagnets. Only the maxima of θ_{AHE} are shown. Whereas the θ_{AHE} of $SmMn_2Ge_2$ is comparable to that of other ferromagnetic materials, its giant AHC is comparable to that of semimetal materials with a topologically nontrivial ground state such as Fe_3GeTe_2 [65], GdPtBi [66], and $Co_3Sn_2S_2$ [4]. Thus, $SmMn_2Ge_2$ represents a new Hall material with high conductivity.

We now turn to the origin of the THE in $SmMn_2Ge_2$. The present results showed that $SmMn_2Ge_2$ compound exhibits a characteristic field dependence of extracted ρ^T_{xy} at various temperatures above 140 K. Theoretically, the THE is associated with the chirality-induced Berry phase, i.e., it is induced by local scalar spin chirality when itinerant electrons traverse a spin texture of a noncoplanar magnet [72]. It has been established that the nonlinear spin configuration of skyrmions can generate a scalar spin chirality, which brings about a Berry phase and then contributes to the additional Hall signal of THE [17]. To interpret the THE obtained from the Hall effect measurements for $H//c$, we performed real-space observations of their magnetic field-dependent domain evolution processes at room temperature by LTEM. The magnetic field was applied along the out-of-plane direction of sample. Selected-area electron diffraction (SAED) analysis [inset of Fig. 6(a)] reveals that the out-of-plane direction of the sample is along [001] orientation of the single crystal, which agrees well with the arrangement of atoms of the (001) crystal plane [Fig. 1(d)]. Figure 6(a) shows a typical Lorentz image of the single crystal captured at room temperature in zero field. The image shows spontaneous stripelike domains. Such stripe domains possess a long-period helimagnetic structure and the corresponding helix period was determined to be 340 nm based on measurements of the sinusoidal variation of the Lorentz TEM contrast. The helix period length is comparable to that of other RMn_2Ge_2 compounds [28].

Bubble domains are also observed in Lorentz TEM images of the single crystal in addition to the stripelike domains (Figs. 6(a) and S7a-c [33]). However, they are rare and randomly distributed. To increase the density of bubble domains at room temperature, the single crystal was field-cooled (FC) using a protocol described elsewhere [28,73,74]. As schematically shown in Fig. 6(b), the single crystal was heated first to a temperature above Tc in zero magnetic field followed by cooling down to 300 K in a magnetic field of 0.05 T. As shown in Fig. S7d [33], LTEM imaging reveals a high density of the bubbles after cooling from a high temperature to 300 K. The bubbles are arranged into a quasiregular pattern. When the single crystal was tilted by an angle (θ) from the normal of the surface, the contrast of the bubble domains was improved significantly. As illustrated in Figs. S7d-f [33], the bubbles show distinct contrast relative to the surrounding matrix at an angle of 17.2°. They were determined to have a mean diameter of 0.43 μm. The bubbles obtained by zero-field cooling are extremely stable. They persisted even after the single crystal was exposed to air for several days at room temperature. This high stability of the bubbles means that $SmMn_2Ge_2$ is promising for applications in nonvolatile magnetic memory devices.

The density and size of the bubble domains decrease in a higher magnetic field. The bubbles vanish at a magnetic field of approximately 0.1 T, at which the single crystal dwells in a ferromagnetic state [Figs. 6(d)–6(g)]. It should be mentioned that the skyrmionic type and trivial bubbles coexist. The LTEM images of the skyrmionic bubbles generally show a symmetric contrast variation (bubble "h"), that is,

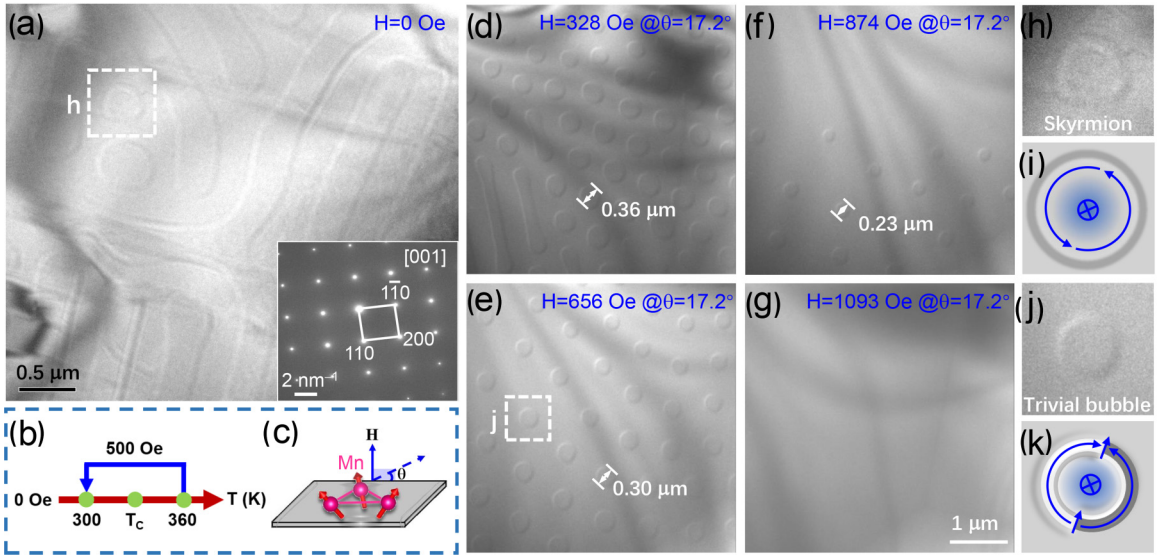

FIG. 6. (a) LTEM images showing magnetic domains in zero field. The inset shows the SAED pattern. (b) Schematic drawing of field-cooling procedure. (c) Schematic illustration of noncoplanar configuration of canted spins of Mn atoms. (d)–(g) LTEM images taken in different external magnetic fields at 300 K. Enlarged views of (h) bubble "h" and (j) bubble "j" enclosed by a dashed box. (i) (k) Schematic drawings showing a Bloch-type skyrmionic-type and a trivial-type bubble corresponding to the spin configuration of bubble "h" and bubble "j", respectively.

dark-white-gray-white-dark along a diameter direction [Fig. 6(h)]. The skyrmionic bubble has a topological number of Ns $= \pm 1$. Some of the bubbles show an asymmetric contrast variation (bubble "j"), white-dark-gray-white-dark, along their diameters [Fig. 6(j)], indicating that they are of a trivial type. These bubbles are composed of a pair of nonconvergent Bloch lines with a topological number of $N_s = 0$. These two types of bubbles are further explained in Figs. 6(i) and 6(k). The trivial bubbles consist of a pair of nonconvergent semicircular arc, whereas the skyrmionics-type bubbles form a ringlike pattern. The coexistence of different bubbles has also been observed in other centrosymmetric magnetic systems such as Fe_3Sn_2 [21] and MnNiGa [40]. It can be understood because a centrosymmetric magnet like $SmMn_2Ge_2$ possesses two degrees of freedom, i.e., vorticity and helicity, which makes the skyrmionics-type bubbles to coexist with the topologically trivial bubbles. In terms of these observations, the THE of the single crystal can be related to the formation of skyrmionic-type bubbles whereas the trivial bubbles are associated with the noncoplanar spin configurations of the canted Mn atoms, as schematically depicted in Fig. 6(c).

V. CONCLUSION

We have unraveled multiple unconventional Hall responses, i.e., the coexistence of a giant AHE and robust THE, in high-quality single crystals of $SmMn_2Ge_2$. A giant AHE of 1715 Ω^{-1} cm^{-1} has been observed for $H//a$ and $I\backslash text\{//\}b$. The giant AHE has been attributed to an extrinsically controlled mechanism, skew-scattering by conical spin-clusters with scalar spin chirality. A THE has been observed for $H//c$ and attributed to skyrmionics bubbles in real space following the LTEM investigation. In addition, the measurements of the angular dependence Hall effect with the magnetic field rotating about the a or the c axis have revealed a PTHE, which vanishes at low temperature due to the FM to AFM transition. The PTHE has been attributed to the nonzero spin chirality induced by the noncoplanar spin textures of Mn atoms. The discovery of the coexistence of the multiple unusual electronic transport effects makes $SmMn_2Ge_2$ promising for multifunctional applications in spintronic devices. Our work should motivate the search of new magnetic topological materials with noncoplanar spin textures showing multiple anomalous transport properties.

ACKNOWLEDGMENTS

This work was financially supported by the National Key R&D Program of China (Grant No. 2022YFA1402600) and the National Natural Science Foundation of China (Grants No. 51831003, No. 52161135108, and No. 12274321). A portion of this work was carried out at the Synergetic Extreme Condition User Facility (SECUF) in Huairou Science City, Beijing.

[1] S. Nakatsuji, N. Kiyohara, and T. Higo, Large anomalous Hall effect in a noncollinear antiferromagnet at room temperature, Nature (London) **527**, 212 (2015).

[2] A. K. Nayak, J. E. Fischer, Y. Sun, B. Yan, J. karel, A. C. Komarek, C. Shekhar, N. Kumar, W. Schnelle, J. Kübler *et al.*, Large anomalous Hall effect driven by a nonvanishing Berry curvature in the noncolinear antiferromagnet Mn_3Ge, Sci. Adv. **2**, e1501870 (2016).

[3] Z. Wang, M. G. Vergniory, S. Kushwaha, M. Hirschberger, E. V. Chulkov, A. Ernst, N. P. Ong, R. J. Cava, and B. A. Bernevig, Time-reversal-breaking Weyl fermions in magnetic Heusler alloys, Phys. Rev. Lett. **117**, 236401 (2016).

[4] E. Liu, Y. Sun, N. Kumar, L. Muechler, A. Sun, J. Lin, S. Y. Yang, D. Liu, A. Liang, Q. Xu *et al.*, Giant anomalous Hall effect in a ferromagnetic kagome-lattice semimetal, Nat. Phys. **14**, 1125 (2018).

[5] M. Imada, A. Fujimori, and Y. Tokura, Metal-insulator transitions, Rev. Mod. Phys. **70**, 1039 (1998).

[6] F. Narita and M. Fox, A review on piezoelectric, magnetostrictive, and magnetoelectric materials and device technologies for energy harvesting applications, Adv. Eng. Mater. **20**, 1700743 (2018).

[7] N. Nagaosa, J. Sinova, S. Onoda, A. H. MacDonald, and N. P. Ong, Anomalous Hall effect, Rev. Mod. Phys. **82**, 1539 (2010).

[8] Y. Fujishiro, N. Kanazawa, R. Kurihara, H. Ishizuka, T. Hori, F. S. Yasin, X. Yu, A. Tsukazaki, M. Ichikawa, M. Kawasaki *et al.*, Giant anomalous Hall effect from spin-chirality scattering in a chiral magnet, Nat. Commun. **12**, 317 (2021).

[9] A. Sakai, Y. P. Mizuta, A. A. Nugroho, R. Sihombing, T. Koretsune, M. Suzuki, N. Takemori, R. Ishii, D. Nishio-Hamane, R. Arita *et al.*, Giant anomalous Nernst effect and quantum-critical scaling in a ferromagnetic semimetal, Nat. Phys. **14**, 1119 (2018).

[10] P. Li, J. Koo, W. Ning, J. Li, L. Miao, L. Min, Y. Zhu, Y. Wang, N. Alem, C. X. Liu *et al.*, Giant room temperature anomalous Hall effect and tunable topology in a ferromagnetic topological semimetal Co_2MnAl, Nat. Commun. **11**, 3476 (2020).

[11] H. Li, B. Zhang, J. Liang, B. Ding, J. Chen, J. Shen, Z. Li, E. Liu, X. Xi, G. Wu *et al.*, Large anomalous Hall effect in a hexagonal ferromagnetic Fe_5Sn_3 single crystal, Phys. Rev. B **101**, 140409(R) (2020).

[12] S. N. Guin, Q. Xu, N. Kumar, H. H. Kung, S. Dufresne, C. Le, P. Vir, M. Michiardi, T. Pedersen, S. Gorovikov *et al.*, 2D-Berry-curvature-driven large anomalous Hall effect in layered topological nodal-line MnAlGe, Adv. Mater. **33**, 2006301 (2021).

[13] S. Onoda, N. Sugimoto, and N. Nagaosa, Intrinsic versus extrinsic anomalous Hall effect in ferromagnets, Phys. Rev. Lett. **97**, 126602 (2006).

[14] H. Ishizuka and N. Nagaosa, Spin chirality induced skew scattering and anomalous Hall effect in chiral magnets, Sci. Adv. **4**, eaap9962 (2018).

[15] S. Y. Yang, Y. Wang, B. R. Ortiz, D. Liu, J. Gayles, E. Derunova, R. Gonzalez-Hernandez, L. Šmejkal, Y. Chen, S. S. P. Parkin *et al.*, Giant, unconventional anomalous Hall effect in the metallic frustrated magnet candidate, KV_3Sb_5, Sci. Adv. **6**, eabb6003 (2020).

[16] G. Kimbell, C. Kim, W. Wu, M. Cuoco, and J. W. A. Robinson, Challenges in identifying chiral spin textures via the topological Hall effect, Commun. Mater. **3**, 19 (2022).

[17] A. N. Bogdanov and C. Panagopoulos, Physical foundations and basic properties of magnetic skyrmions, Nat. Rev. Phys. **2**, 492 (2020).

[18] A. Fert, N. Reyren, and V. Cros, Magnetic skyrmions: Advances in physics and potential applications, Nat. Rev. Mater. **2**, 17031 (2017).

[19] W. Jiang, G. Chen, K. Liu, J. Zang, S. G. E. te Velthuis, and A. Hoffmann, Skyrmions in magnetic multilayers, Phys. Rep. **704**, 1 (2017).

[20] X. Z. Yu, Y. Onose, N. Kanazawa, J. H. Park, J. H. Han, Y. Matsui, N. Nagaosa, and Y. Tokura, Real-space observation of a two-dimensional skyrmion crystal, Nature (London) **465**, 901 (2010).

[21] Z. Hou, W. Ren, B. Ding, G. Xu, Y. Wang, B. Yang, Q. Zhang, Y. Zhang, E. Liu, F. Xu *et al.*, Observation of various and spontaneous magnetic skyrmionic bubbles at room temperature in a frustrated kagome magnet with uniaxial magnetic anisotropy, Adv. Mater. **29**, 1701144 (2017).

[22] J. X. Yin, S. S. Zhang, H. Li, K. Jiang, G. Chang, B. Zhang, B. Lian, C. Xiang, I. Belopolski, H. Zheng *et al.*, Giant and anisotropic many-body spin–orbit tunability in a strongly correlated kagome magnet, Nature (London) **562**, 91 (2018).

[23] G. Gong, L. Xu, Y. Bai, Y. Wang, S. Yuan, Y. Liu, and Z. Tian, Large topological Hall effect near room temperature in noncollinear ferromagnet $LaMn_2Ge_2$ single crystal, Phys. Rev. Mater. **5**, 034405 (2021).

[24] S. Wang, Q. Zeng, D. Liu, H. Zhang, L. Ma, G. Xu, Y. Liang, Z. Zhang, H. Wu, R. Che *et al.*, Giant topological Hall effect and superstable spontaneous skyrmions below 330 K in a centrosymmetric complex noncollinear ferromagnet $NdMn_2Ge_2$, ACS Appl. Mater. Interfaces **12**, 24125 (2020).

[25] X. Zheng, X. Zhao, J. Qi, X. Luo, S. Ma, C. Chen, H. Zeng, G. Yu, N. Fang, S. U. Rehman *et al.*, Giant topological Hall effect around room temperature in noncollinear ferromagnet $NdMn_2Ge_2$ single crystal, Appl. Phys. Lett. **118**, 072402 (2021).

[26] L. Xu, Y. Bai, G. Gong, F. Song, Z. Li, Y. Han, L. Ling, and Z. Tian, Strong anisotropic Hall effect in single-crystalline $CeMn_2Ge_2$ with helical spin order, Phys. Rev. B **105**, 075108 (2022).

[27] D. Huang, H. Li, B. Ding, X. Xi, Y. C. Lau, and W. Wang, Enhanced magnetic anisotropy induced by praseodymium ferromagnetic order and anomalous transport properties in $PrMn_2Ge_2$ single crystals, Phys. Rev. B **107**, 224417 (2023).

[28] Z. Hou, L. Li, C. Liu, X. Gao, Z. Ma, G. Zhou, Y. Peng, M. Yan, X. X. Zhang, and J. Liu, Emergence of room temperature stable skyrmionic bubbles in the rare earth based $REMn_2Ge_2$ (RE = Ce, Pr, and Nd) magnets, Mater. Today Phys. **17**, 100341 (2021).

[29] H. Fujii, T. Okamoto, T. Shigeoka, and N. Iwata, Reentrant ferromagnetism observed in $SmMn_2Ge_2$, Solid State Commun. **53**, 715 (1985).

[30] G. J. Tomka, C. Ritter, P. C. Riedi, C. Kapusta, and W. Kocemba, Magnetic structure of $^{154}SmMn_2Ge_2$ as a function of temperature and pressure, Phys. Rev. B **58**, 6330 (1998).

[31] Q. Hou, M. Song, X. Xu, Y. Wang, C. Dong, Y. Feng, M. He, Y. Liu, L. Cao, J. Wang *et al.*, Critical behavior in the itinerant ferromagnet $SmMn_2Ge_2$, Chin. Phys. B **32**, 087501 (2023).

[32] X. Y. Wang, J. F. Lin, X. Y. Zeng, H. Wang, X. P. Ma, Y. T. Wang, K. Han, and T. L. Xia, Multiple magnetic phase transitions and critical behavior in single-crystal $SmMn_2Ge_2$, Chin. Phys. Lett. **40**, 067503 (2023).

[33] See Supplemental Material at http://link.aps.org/supplemental/10.1103/PhysRevB.109.144406 for the energy-dispersive spectroscopy analysis results (Fig. S1). Crystalline structure, various crystal planes and the diffraction spots of $SmMn_2Ge_2$ single crystal (Table S1 and Fig. S2). Hall resistivity and Hall conductivity with $H//a$ axis (Fig. S3). Hall resistivity and Hall conductivity and method for extracting the topological Hall resistivity with $H//c$ axis (Fig. S4). Measurements on a second single crystal for the authenticity of a large AHE (Fig. S5).

Analysis of the anomalous Hall conductivity for $H//c$ (Fig. S6). The magnetic domain of $SmMn_2Ge_2$ single crystal revealed using LTEM (Fig. S7).

[34] D. Huang, H. Li, B. Ding, X. Xi, J. Gao, Y. C. Lau, and W. Wang, Plateaulike magnetoresistance and topological Hall effect in Kagome magnets $TbCo_2$ and $DyCo_2$, Appl. Phys. Lett. **121**, 232404 (2022).

[35] N. P. Kolmakova, A. A. Sidorenko, and R. Z. Levitin, Features of the magnetic properties of rare-earth intermetallides RMn_2Ge_2, Low Temp. Phys. **28**, 653 (2002).

[36] M. T. Johnson, P. J. H. Bloemen, F. J. A. d. Broeder, and J. J. d. Vries, Magnetic anisotropy in metallic multilayers, Rep. Prog. Phys. **59**, 1409 (1996).

[37] D. Chen, C. Le, C. Fu, H. Lin, W. Schnelle, Y. Sun, and C. Felser, Large anomalous Hall effect in the kagome ferromagnet $LiMn_6Sn_6$, Phys. Rev. B **103**, 144410 (2021).

[38] B. He, Y. Wang, M. Q. Arguilla, N. D. Cultrara, M. R. Scudder, J. E. Goldberger, W. Windl, and J. P. Heremans, The Fermi surface geometrical origin of axis-dependent conduction polarity in layered materials, Nat. Mater. **18**, 568 (2019).

[39] Y. Wang and P. Narang, Anisotropic scattering in the goniopolar metal $NaSn_2As_2$, Phys. Rev. B **102**, 125122 (2020).

[40] W. Wang, Y. Zhang, G. Xu, L. Peng, B. Ding, Y. Wang, Z. Hou, X. Zhang, X. Li, E. Liu *et al.*, A centrosymmetric hexagonal magnet with superstable biskyrmion magnetic nanodomains in a wide temperature range of 100 K to 340 K, Adv. Mater. **28**, 6887 (2016).

[41] H. Li, B. Ding, J. Chen, Z. Li, Z. Hou, E. Liu, H. Zhang, X. Xi, G. Wu, and W. Wang, Large topological Hall effect in a geometrically frustrated kagome magnet Fe_3Sn_2, Appl. Phys. Lett. **114**, 192408 (2019).

[42] A. Neubauer, C. Pfleiderer, B. Binz, A. Rosch, R. Ritz, P. G. Niklowitz, and P. Boni, Topological Hall effect in the A phase of MnSi, Phys. Rev. Lett. **102**, 186602 (2009).

[43] N. Kanazawa, Y. Onose, T. Arima, D. Okuyama, K. Ohoyama, S. Wakimoto, K. Kakurai, S. Ishiwata, and Y. Tokura, Large topological Hall effect in a short-period helimagnet MnGe, Phys. Rev. Lett. **106**, 156603 (2011).

[44] P. Vir, J. Gayles, A. S. Sukhanov, N. Kumar, F. Damay, Y. Sun, J. Kübler, C. Shekhar, and C. Felser, Anisotropic topological Hall effect with real and momentum space Berry curvature in the antiskrymion-hosting Heusler compound $Mn_{1.4}PtSn$, Phys. Rev. B **99**, 140406(R) (2019).

[45] W. Zhang, B. Balasubramanian, A. Ullah, R. Pahari, X. Li, L. Yue, S. R. Valloppilly, A. Sokolov, R. Skomski, and D. J. Sellmyer, Comparative study of topological Hall effect and skyrmions in NiMnIn and NiMnGa, Appl. Phys. Lett. **115**, 172404 (2019).

[46] Z. H. Liu, Y. J. Zhang, G. D. Liu, B. Ding, E. K. Liu, H. M. Jafri, Z. P. Hou, W. H. Wang, X. Q. Ma, and G. H. Wu, Transition from anomalous Hall effect to topological Hall effect in hexagonal noncollinear magnet Mn_3Ga, Sci. Rep. **7**, 515 (2017).

[47] P. K. Rout, P. V. Prakash Madduri, S. K. Manna, and A. K. Nayak, Field-induced topological Hall effect in the noncoplanar triangular antiferromagnetic geometry of Mn_3Sn, Phys. Rev. B **99**, 094430 (2019).

[48] J. Kübler and C. Felser, Non-collinear antiferromagnets and the anomalous Hall effect, Europhys. Lett. **108**, 67001 (2014).

[49] Y. You, Y. Gong, H. Li, Z. Li, M. Zhu, J. Tang, E. Liu, Y. Yao, G. Xu, F. Xu, and W. Wang, Angular dependence of the topological Hall effect in the uniaxial van der Waals ferromagnet Fe_3GeTe_2, Phys. Rev. B **100**, 134441 (2019).

[50] H. Li, B. Ding, J. Chen, Z. Li, E. Liu, X. Xi, G. Wu, and W. Wang, Large anisotropic topological Hall effect in a hexagonal noncollinear magnet Fe_5Sn_3, Appl. Phys. Lett. **116**, 182405 (2020).

[51] Q. Wang, K. J. Neubauer, C. Duan, Q. Yin, S. Fujitsu, H. Hosono, F. Ye, R. Zhang, S. Chi, K. Krycka *et al.*, Field-induced topological Hall effect and double-fan spin structure with a c-axis component in the metallic kagome antiferromagnetic compound YMn_6Sn_6, Phys. Rev. B **103**, 014416 (2021).

[52] C. Liu, H. Zhang, Z. Li, Y. Yan, Y. Zhang, Z. Hou, and X. Fu, Nontrivial spin textures induced remarkable topological Hall effect and extraordinary magnetoresistance in kagome magnet $TmMn_6Sn_6$, Surf. Interfaces **39**, 102866 (2023).

[53] N. Mohanta, S. Okamoto, and E. Dagotto, Planar topological Hall effect from conical spin spirals, Phys. Rev. B **102**, 064430 (2020).

[54] Y. Wang, J. Yan, J. Li, S. Wang, M. Song, J. Song, Z. Li, K. Chen, Y. Qin, L. Ling *et al.*, Magnetic anisotropy and topological Hall effect in the trigonal chromium tellurides Cr_5Te_8, Phys. Rev. B **100**, 024434 (2019).

[55] X. Y. Wang, S. Xu, H. Wang, J. F. Lin, X. Y. Zeng, X. P. Ma, J. Gong, Y. T. Wang, K. Han, and T. L. Xia, Uniaxial magnetic anisotropy and anomalous Hall effect in the ferromagnetic compound $PrMn_2Ge_2$, Phys. Rev. B **107**, 144402 (2023).

[56] N. Kumar, S. N. Guin, C. Felser, and C. Shekhar, Planar Hall effect in the Weyl semimetal GdPtBi, Phys. Rev. B **98**, 041103(R) (2018).

[57] P. Li, C. H. Zhang, J. W. Zhang, Y. Wen, and X. X. Zhang, Giant planar Hall effect in the Dirac semimetal $ZrTe_{5-\delta}$, Phys. Rev. B **98**, 121108(R) (2018).

[58] T. McGuire and R. Potter, Anisotropic magnetoresistance in ferromagnetic 3d alloys, IEEE Trans. Magn. **11**, 1018 (1975).

[59] A. W. Rushforth, K. Výborný, C. S. King, K. W. Edmonds, R. P. Campion, C. T. Foxon, J. Wunderlich, A. C. Irvine, P. Vašek, V. Novák *et al.*, Anisotropic magnetoresistance components in (Ga, Mn)As, Phys. Rev. Lett. **99**, 147207 (2007).

[60] Y. Tian, L. Ye, and X. Jin, Proper scaling of the anomalous Hall effect, Phys. Rev. Lett. **103**, 087206 (2009).

[61] J. Smit, The spontaneous Hall effect in ferromagnetics II, Physica **24**, 39 (1958).

[62] L. Berger, Side-jump mechanism for the Hall effect of ferromagnets, Phys. Rev. B **2**, 4559 (1970).

[63] R. Karplus and J. M. Luttinger, Hall effect in ferromagnetics, Phys. Rev. **95**, 1154 (1954).

[64] T. Miyasato, N. Abe, T. Fujii, A. Asamitsu, S. Onoda, Y. Onose, N. Nagaosa, and Y. Tokura, Crossover behavior of the anomalous Hall effect and anomalous Nernst effect in itinerant ferromagnets, Phys. Rev. Lett. **99**, 086602 (2007).

[65] K. Kim, J. Seo, E. Lee, K. T. Ko, B. S. Kim, B. G. Jang, J. M. Ok, J. Lee, Y. J. Jo, W. Kang *et al.*, Large anomalous Hall current induced by topological nodal lines in a ferromagnetic van der Waals semimetal, Nat. Mater. **17**, 794 (2018).

[66] T. Suzuki, R. Chisnell, A. Devarakonda, Y. T. Liu, W. Feng, D. Xiao, J. W. Lynn, and J. G. Checkelsky, Large anomalous Hall effect in a half-Heusler antiferromagnet, Nat. Phys. **12**, 1119 (2016).

[67] S. Onoda, N. Sugimoto, and N. Nagaosa, Quantum transport theory of anomalous electric, thermoelectric, and thermal Hall effects in ferromagnets, Phys. Rev. B **77**, 165103 (2008).

[68] C. Zeng, Y. Yao, Q. Niu, and H. H. Weitering, Linear magnetization dependence of the intrinsic anomalous Hall effect, Phys. Rev. Lett. **96**, 037204 (2006).

[69] L. Ye, M. Kang, J. Liu, F. von Cube, C. R. Wicker, T. Suzuki, C. Jozwiak, A. Bostwick, E. Rotenberg, D. C. Bell *et al.*, Massive Dirac fermions in a ferromagnetic kagome metal, Nature (London) **555**, 638 (2018).

[70] N. Manyala, Y. Sidis, J. F. DiTusa, G. Aeppli, D. P. Young, and Z. Fisk, Large anomalous Hall effect in a silicon-based magnetic semiconductor, Nat. Mater. **3**, 255 (2004).

[71] C. Surgers, G. Fischer, P. Winkel, and H. V. Lohneysen, Large topological Hall effect in the noncollinear phase of an antiferromagnet, Nat. Commun. **5**, 3400 (2014).

[72] P. Bruno, V. K. Dugaev, and M. Taillefumier, Topological Hall effect in magnetic nanostructures, Phys. Rev. Lett. **93**, 096806 (2004).

[73] C. Zhang, C. Liu, J. Zhang, Y. Yuan, Y. Wen, Y. Li, D. Zheng, Q. Zhang, Z. Hou, G. Yin *et al.*, Room-temperature magnetic skyrmions and large topological Hall effect in chromium telluride engineered by self-intercalation, Adv. Mater. **35**, 2205967 (2023).

[74] B. Ding, X. Li, Z. Li, X. Xi, Y. Yao, and W. Wang, Tuning the density of zero-field skyrmions and imaging the spin configuration in a two-dimensional Fe_3GeTe_2 magnet, NPG Asia Mater. **14**, 74 (2022).